Investigation of the Ahmed body cross-wind flow topology by robotic volumetric PIV

Sciacchitano, Andrea; Giaquinta, Daniele

DOI
10.18726/2019_3

Publication date
2019

Document Version
Final published version

Published in
Proceedings of the 13th International Symposium on Particle Image Velocimetry

13th International Symposium on Particle Image Velocimetry – ISPIV 2019
Munich, Germany, July 22-24, 2019

Investigation of the Ahmed body cross-wind flow topology by robotic volumetric PIV

Andrea Sciacchitano[1]*, Daniele Giaquinta[2]

[1] Department of Aerospace Engineering, Delft University of Technology, Delft, The Netherlands

[2] Department of Aerodynamics, Mercedes-AMG Petronas Formula One Team, Brackley, UK

*a.sciacchitano@tudelft.nl

Abstract

Robotic volumetric PIV is employed to investigate the time-averaged three-dimensional near-wake flow topology of the Ahmed body in steady cross-wind conditions. The model selected for this study is a 1:2 replica of the reference Ahmed body with 25° slant angle. The measurements are conducted at free-stream velocity of 12 m/s, resulting in a Reynolds number of 1.15×10^5 based on the model's height. Yaw angles of 0°, 4° and 8° are considered. The results show that the position and strength of the C-pillar vortices are significantly influenced by the presence of a yaw angle. The yaw angles cause an increase in the strength of the windward C-pillar vortex, with a consequent upward displacement; conversely, the strength of the leeward vortex decreases, and the position of its core moves downwards and inboard. At the larger yaw angle, the presence of a ground streamwise vortex is detected which co-rotates with the windward C-pillar vortex and is located between the latter and the ground.

1 Introduction

Advances in automotive research and development have increased the demand for detailed knowledge of the three-dimensional flow field over road vehicles to reduce the aerodynamic drag and thus improve fuel efficiency. The flow over a road vehicle is complex and fully three-dimensional, characterized by large turbulent wakes and longitudinal trailing vortices (Hucho and Sovran, 1993), whose shapes and extensions depend strongly on the vehicle geometry. Because the wake flow has the major contribution to the vehicle aerodynamic drag (up to 80%, Kourta and Gilliéron, 2009), detailed knowledge of the wake flow structure and its relation to the vehicle geometry is critical for the successful design of future cars.

Since its introduction in 1984, the Ahmed reference body (Ahmed et al., 1984) has been widely used as a simplified car model to investigated both experimentally and numerically the salient flow features of ground vehicles' wakes. The Ahmed body comprises three parts: a fore body with rounded edges, where flow separation typically occurs; a middle section composed by a box with rectangular cross section to stabilize the flow; a rear end characterized by a slanted surface. In their seminal paper, Ahmed et al. (1984) propose a topological model for the near-wake flow structure that features two recirculation flow regions situated one over the other, and two longitudinal vortices, denoted as the C-pillar vortices. The former recirculation regions are generated by the shear layers roll-up at the top and bottom edges of the flat vertical base, respectively, whereas the C-pillar vortices are produced by the pressure difference between the flow at the side edges of the model and that on the slanted surface. The strengths of the C-pillar vortices and of the recirculation flow regions are strongly dependent on the base slant angle (Ahmed et al., 1984; Ahmed, 1984). Lienhart and Becker (2003) carried out laser-Doppler velocimetry measurements to provide

accurate velocity profiles up to third order statistical moments in the wake of the Ahmed body for 25° and 35° slant angles. Their results validated Ahmed et al.'s findings and became a benchmark for many CFD simulations (see for instance Krajnović and Davidson, 2005a, 2005b, Minguez et al., 2008). The effect of the slant angle on the wake flow topology was analyzed by Tunay et al. (2014) by planar PIV measurements at relatively low Reynolds number (1.5×10^4 based on the model's height). The authors report that the slope angle of the slanted surface has significant effects on the near wake flow topology; in particular, an increase of the slant angle between 25° and 35° causes the location of the critical flow points (two foci and a saddle point) to move further in the vertical and streamwise directions, yielding a wider wake. Vino et al. (2005) investigated experimentally the time-averaged and time-dependent nature of the Ahmed body near- and far-wake. The study involved the use of 13-hole pressure probe in the wake of the model, surface pressure measurements on the model rear end, surface oil flow visualization, smoke flow visualization and drag measurements by force balance. Contrary to the flow topology model proposed by Ahmed et al. (1984), Vino et al. (2005) showed that in their experiments the separated flow region over the slanted surface does not fully reattach at the end of the slant, but instead mixes with the large separated region behind the vertical base. Wang et al. (2013) conducted planar PIV measurements in three orthogonal planes in the wake of the Ahmed body with and without ground clearance, showing that the lower recirculation region behind the base disappears in absence of ground clearance. Zhang et al. (2015) carried out hot-wire, flow visualization and PIV measurements in the wake of a 25°-slant Ahmed body to characterize the unsteady structures and their corresponding Strouhal numbers in the model wake. More recently, Sellappan et al. (2018) conducted planar PIV, stacked stereoscopic PIV and tomographic PIV measurements in the wake of a 25°-slant Ahmed body to elucidate its near-wake flow topology at $Re = 1.1\times10^6$.

Despite much work has been done to characterize the flow topology in the wake of the Ahmed body in headwind flow conditions, much less investigations are found in the literature that discuss the flow over the Ahmed body in yawed conditions. Bello-Millán et al. (2016) conducted force balance measurements to determine the drag-coefficient of a 25°-slant Ahmed body for yaw angles between 0° and 90°. Surface pressure measurements as well as force balance measurements were performed by Bayraktar et al. (2001) for three different slant angles below the critical value of 30°, and for yawing angles up to ±15°. Keogh et al. (2016) carried out Large Eddy Simulations to assess the flow over an Ahmed body during cornering, and showed that the variable flow angle and acceleration during cornering cause an increase of the size of the outboard C-pillar vortex, and a decrease of the size of the inboard one. Meile et al. (2016) studied the effect of slant and yaw angles on the flow around the Ahmed body via planar PIV, wall pressure and aerodynamic loads measurements. The authors found that the dimension of the C-pillar vortices increases or decreases with their windward or leeward orientation, respectively.

The present work makes use of the recently-introduced robotic volumetric PIV technique (Jux et al., 2018) to provide an unprecedented quantitative measurement of the three-dimensional time-averaged flow topology of the Ahmed body in steady cross-wind conditions.

2 Experimental setup

Experiments are conducted in the Open Jet Facility (OJF) of the TU Delft Aerodynamics Laboratories, which is a closed-loop, open test section wind tunnel with a 3:1 contraction ratio (1.88 linear contraction in width and 1.62 in height) and an octagonal exit section of 2.85×2.85 m^2. The maximum free-stream velocity is 35 m/s with 0.5% turbulence intensity (Lignarolo et al., 2014).

The test model is a 50% replica of the Ahmed reference model with a slant angle of 25°, and measures 522×194.5×144 mm in length, width and height, respectively. The slanted surface is 111 mm long, while the front of the body is rounded with a radius of curvature of 50 mm. Zig-zag stripes are applied all around the frontal part of the body to trigger the boundary layer transition to

the turbulent regime. The model is supported by 4 circular stilts of 15 mm diameter which generate a clearance from the ground of 25 mm. The stilts are connected to a disk that can be rotated in order to reproduce the different yaw angles. Measurements are carried out in headwind condition and at yaw angles of 4° and 8° (counter-clockwise rotation when the model is seen from the top). The free-stream velocity is set to 12 m/s, yielding a Reynolds number of 1.15×10^5 based on the model height. The flow is seeded with neutrally buoyant helium-filled soap bubbles released by a 200-generator 10-wing seeding rake placed in the settling chamber of the wind tunnel. Images of the tracer particles are recorded with a robotic volumetric PIV system (Jux et al., 2018), see Figure 1, which makes use of the concept of Coaxial Volumetric Velocimetry (CVV) introduced by Schneiders et al. (2018). The LaVision MiniShaker S probe is employed, which consists of four CMOS sensor cameras installed into a prismatic body of size w×h×d = 13×9×8 cm^3 and mounted at the small tomographic aperture of 4.3°. The cameras sensors have size of 800×600 px^2, maximum acquisition frequency of 511 Hz at full sensor, 10-bit digital output and 4.8 μm pixel pitch. The sensor size is cropped to 700×420 px^2 to increase the acquisition frequency up to f_{acq} = 700 Hz, thus enabling time-resolved measurements. The cameras objectives have a focal length f = 4 mm and the lens aperture is set to $f\#$ = 8. The nominal optical magnification is 0.01, resulting in a digital image resolution of 0.5 mm/px. The seeding concentration is estimated as C_{HFSB} = 0.3 bubbles/cm^3, yielding a number of particles per pixel of about 0.03 ppp which is below the threshold of 0.05 for accurate Lagrangian particle tracking via the Shake-the-Box algorithm (Schanz et al., 2016). The illumination is provided by a Quantronix Darwin Duo Nd:YLF laser (25 mJ pulse energy at 1 kHz, wavelength of 527 nm) and delivered by a 4 m long optical fiber coupled with the laser beam via a spherical converging lens located at the exit of the laser head. The other end of the fiber is placed at the center of the CVV probe, and features a spherical diverging lens to expand the laser light into a conical illumination volume. Imaging and illumination systems are synchronized via a LaVision Programmable Timing Unit (PTU). Time-resolved sequences of 8,000 images are acquired over a measurement volume of up to 130 liters covering the entire region from the front of the model to 2.2 model heights downstream of the model's base.

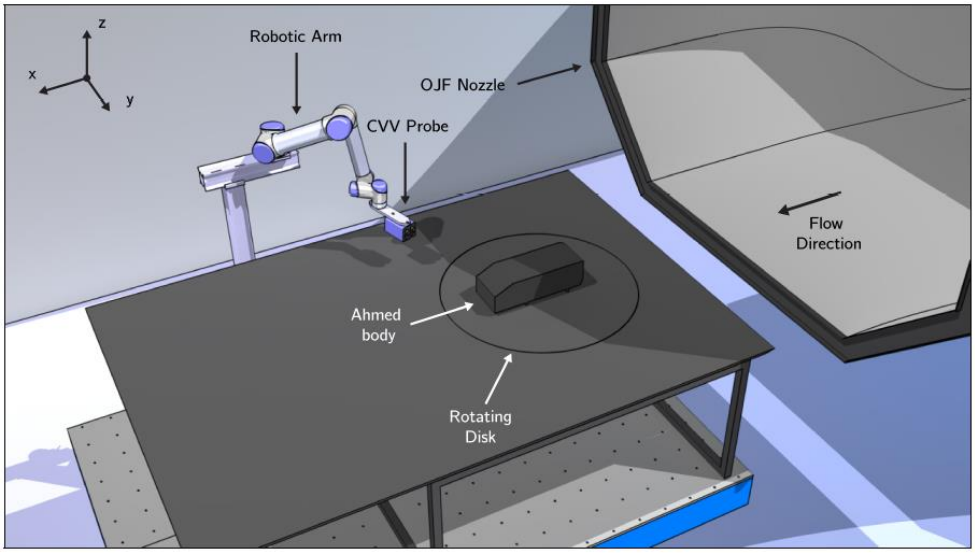

Figure 1: Setup of the robotic PIV measurements.

The background reflections in the raw images are removed via application of a high-pass Butterworth filter (Sciacchitano and Scarano, 2014, see Figure 2), and the pre-processed images are then analyzed via the Shake-the-Box algorithm (STB, Schanz et al., 2016) to retrieve the particles velocities along their trajectories. The instantaneous particle tracks are then averaged in Gaussian-

weighted bins of 20×20×20 mm^3 to determine the time-averaged flow topology (Agüera et al., 2016).

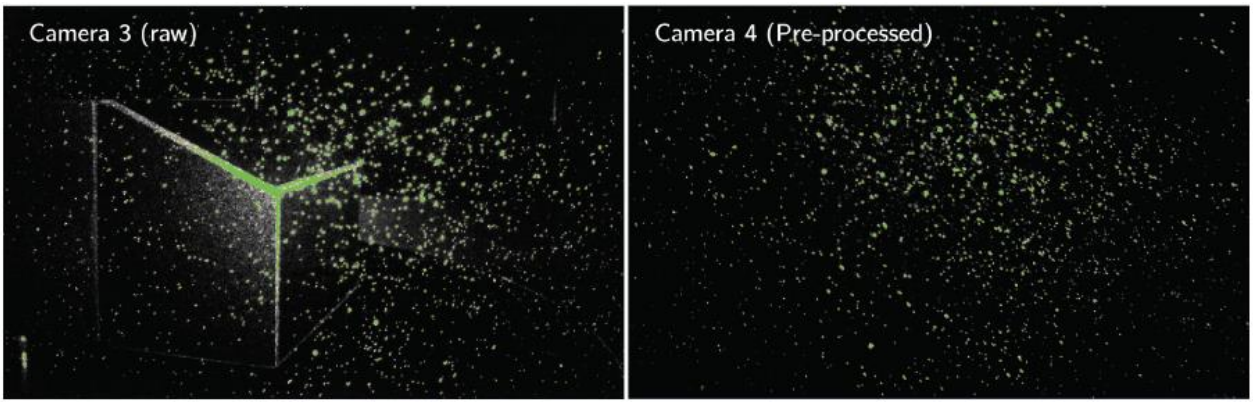

Figure 2. Illustration of sample raw image (left) and image pre-processed via high-pass Butterworth filter (right) for removal of the background reflections.

According to surface base pressure measurements of Vino et al. (2005) at Reynolds numbers between 0.76×10^6 and 2.83×10^6, the Strouhal number associated with the base pressure fluctuations is $St_H \sim 0.4$, which in the present experiment would correspond to a frequency of f_{base} = 33.3 Hz. Considering that 8000 recordings are acquired at acquisition frequency f_{acq} = 700 Hz, the observation period is T_{obs} = 11.43 s, resulting in N_{uncorr} = 381 statistically uncorrelated samples. Assuming maximum fluctuations in the wake of the order of 20% of the free-stream velocity (Lienhart and Backer, 2003), the typical uncertainty at 95% confidence level of the mean velocity is estimated in the order of 0.25 m/s or 2.0% of the free-stream velocity, resulting in a dynamic velocity range (*DVR*, Adrian, 1997) of 50.

3 Results

The flow in the plane y = 0, which corresponds to the symmetry plane for headwind flow conditions, is illustrated in Figure 3 for the three yaw angles of 0, 4 and 8 degrees. As discussed by Tunay et al. (2014) for the β = 0° case, the flow field in such plane is characterized by three critical points, namely two focal points and a saddle point. The upper focal point, indicated with F_1, corresponds to the center of a large recirculation region behind the base of the model, which is fed by the high velocity coming from the slanted surface. Its location is around x/H = 0.25-0.29 and z/H = 0.5, and moves upwards with increasing yaw angle. The lower focal point, indicated with F_2, is located around z/H = 0.2-0.3 and corresponds to a smaller vortex fed by the high velocity at the bottom of the model. While the presence of this focal point is not evident for the cases β = 0° and β = 4° due to the relative large size of the statistical bin element (l_{bin}/H = 0.14), the lower vortex becomes clearly visible for the largest yaw angle measured in this work. At all yaw angles, a saddle point (S) is formed at the location where the streamlines coming from the top of the model meet those coming from the bottom; such critical point, located at a distance of about 0.5-0.6 H from the model base, moves upwards with increasing yaw angle. The positions of the critical points at β = 0° are consistent with those reported by Lienhart and Becker (2003) via LDV measurements, although the latter authors report that all critical points are closer to the Ahmed body base by up to 0.15 H. Such difference is attributed to the higher Reynolds number ($Re_H = 7.7\times10^5$) at which Lienhart and Becker's investigation was conducted.

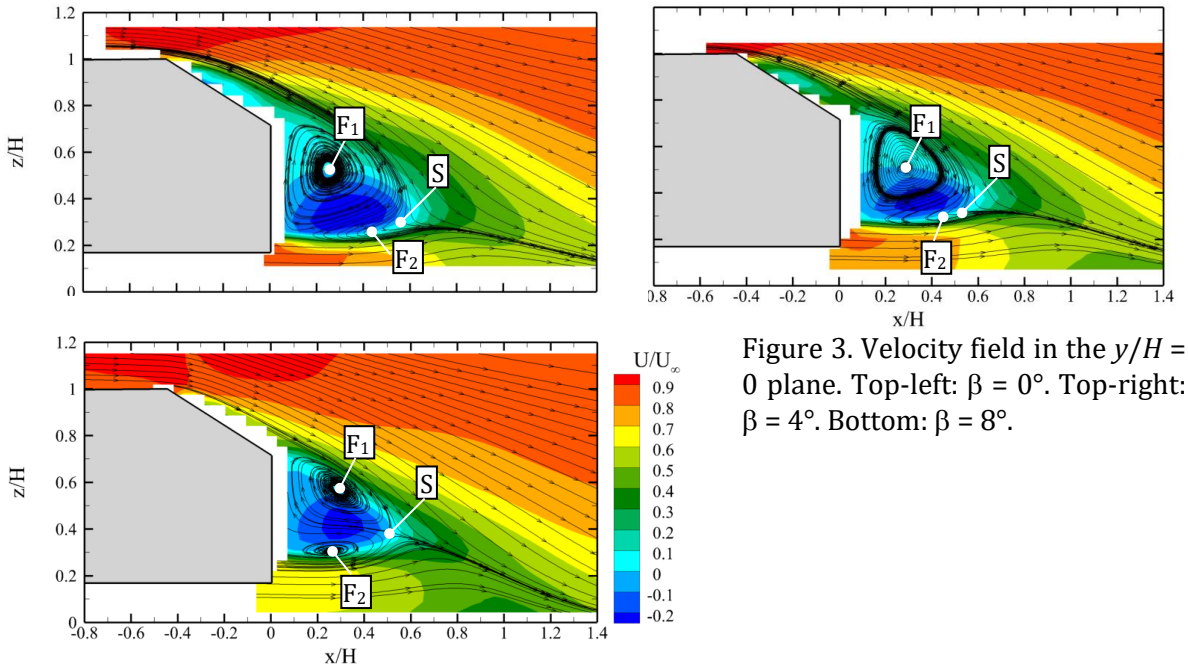

Figure 3. Velocity field in the y/H = 0 plane. Top-left: β = 0°. Top-right: β = 4°. Bottom: β = 8°.

The three-dimensional flow topology in the near wake of the Ahmedy body is presented in Figure 4. The case of zero yaw angle (β = 0°) is analyzed first. A recirculation region is formed on the slanted surface due to the flow separation occurring at the slope discontinuity, as also reported in Sellappan et al. (2018). Two streamwise vortices, known as the C-pillar vortices (Ahmed et al., 1984), originate from the slant side-edges due to the pressure difference between the model side walls and the low-pressure slant surface. The C-pillar vortices induce a downwash above the slanted surface and in the model near wake, thus promoting the flow reattachment on the slanted surface. When moving from the model side edges towards the median plane, the reattachment point location on the slanted surface moves downstream as a result of the weaker downwash induced by the C-pillar vortices. Behind the base of the model, a toroidal vortex is formed due to the velocity difference between the relatively high-speed flow at the top, bottom and sides of the model, and the low-speed region in the near wake. Such toroidal recirculation region extends up to x/H = 0.6.

Under the effect of the low pressure inside the wake recirculation region and of their own downwash, the C-pillar vortices move downwards and closer to each other, consistently with what reported in literature (see e.g. Vino et al., 2005). For the headwind case (β = 0°), the two C-pillar vortices are symmetrical both in shape and intensity. The introduction of a yaw angle breaks the symmetry in the flow field around and downstream of the model. In particular, the static pressure on the right (windward) wall increases and that on the left (leeward) wall decreases with respect to the headwind case. Close to the slant side-edges, this pressure difference affects the C-pillar vortices roll-up, yielding a stronger windward vortex and a weaker leeward vortex (see Figure 4 top-right and bottom), consistently with the surface pressure measurements conducted by Meile et al. (2016). In particular, the peak vorticity of the windward vortex increases by over 10% and 20% for β = 4° and 8°, respectively, whereas that of the leeward vortex decreases by approximately the same amount. As a consequence of the different strength of the C-pillar vortices, the recirculation region on the slanted surface becomes asymmetric, with the windward side featuring attached flow, whereas the leeward side exhibits a larger separation than in the β = 0° case. The toroidal vortex behind the model base, instead, exhibits little variations with the yaw angle.

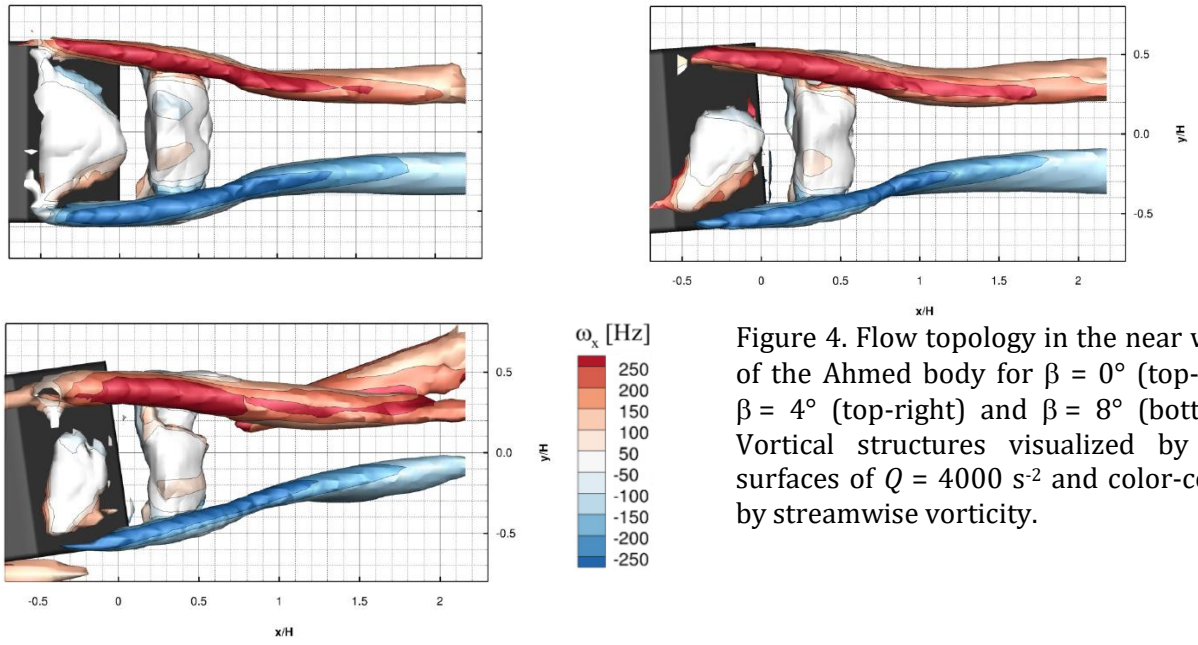

Figure 4. Flow topology in the near wake of the Ahmed body for β = 0° (top-left), β = 4° (top-right) and β = 8° (bottom). Vortical structures visualized by iso-surfaces of Q = 4000 s^{-2} and color-coded by streamwise vorticity.

To investigate more in detail the effect of cross-wind on the near-wake flow field of the Ahmed body and in particular on the C-pillar vortices, the velocity vectors and streamwise vorticity component are illustrated in Figure 5 at x/H = 0.5, 1, 1.5 and 2 and for the three yaw angles. Considering the headwind case (β = 0°) first, the presence of two strong C-pillar vortices can be seen at x/H = 0.5, whose bottom part is deflected inboard as a result of the low pressure in the recirculation region downstream of the base. Below the C-pillars, two weaker counter-rotating vortices originate from the bottom corners of the base of the model. At x/H = 1, the vorticity contours of the two C-pillar vortices assume an elliptical cross section as a result of the interaction with the shear layers from the side walls. Further downstream, the C-pillar vortices move closer to the median plane and are drawn downwards by their own downwash, starting to interact with the ground around x/H = 2. As discussed before, in presence of cross-flow the right (windward) vortex features higher strength than the left (leeward) vortex. As a result, the former tends to remain at higher location than the latter, and causes the leeward vortex to move downward. Such behavior is evident both at β = 4° and β = 8°, with the latter case showing higher differences in position and strength between the two vortices. Also the two induced vortices below the C-pillars at x/H = 0.5 show a clear asymmetry, with the vortex on the windward side being stronger than that on the leeward side. For β = 8°, it is noticed that beyond x/H = 1 the windward C-pillar vortex interacts with another co-rotating vortex located below the former, causing a further increase of its strength. The origin of such vortex is discussed further in the reminder.

The position of the two C-pillar vortices is clearly affected by the presence of the cross-flow. Due to its higher circulation, the windward vortex moves upwards and induces a stronger downwash to the leeward vortex, which is drawn downwards, as summarized in Figure 6-left. Apart from this vertical displacement, also an asymmetry in the y-direction is noticed, being the leeward vortex drawn slightly inboard by the higher suction of the windward vortex (Figure 6-right).

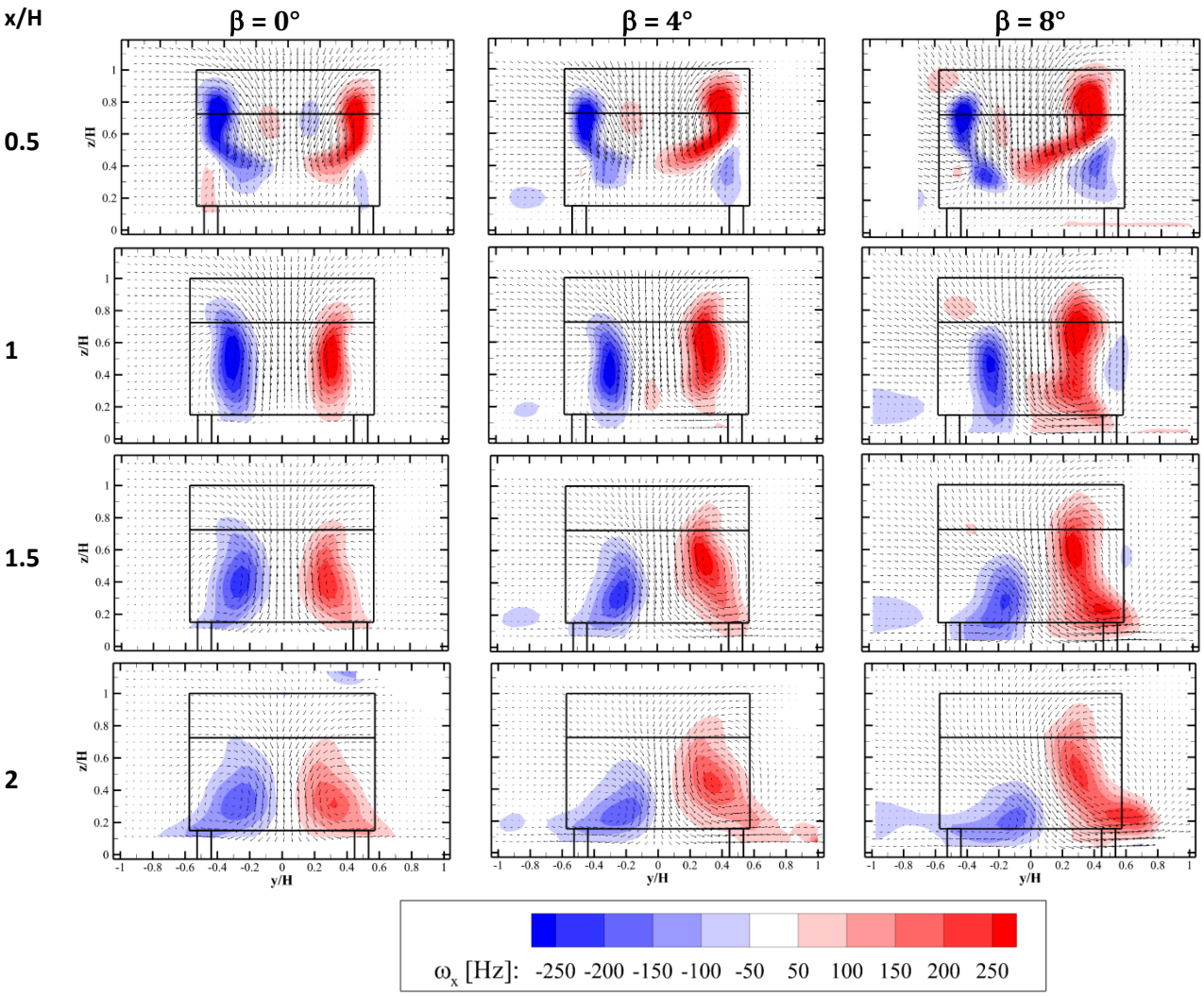

Figure 5. Velocity vectors and streamwise vorticity component in the near wake of the Ahmed body.

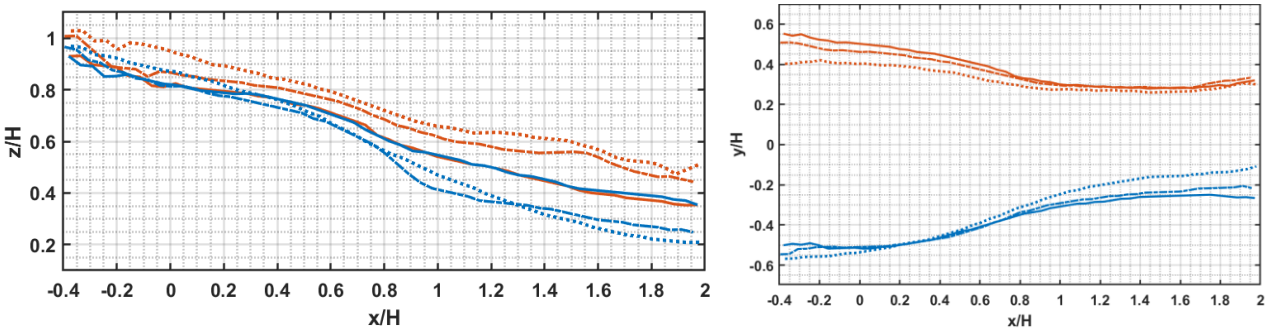

Figure 6. Positions of the cores of the C-pillar vortices in the *xz* plane (left) and the *xy* plane (right). Red curves: right (windward) vortex. Blue curves: left (leeward) vortex. Continuous line: β = 0°. Dash-dotted line: β = 4°. Dotted line: β = 8°.

The iso-surfaces of streamwise vorticity show the presence of two additional streamwise vortices located between the two C-pillar vortices and counter-rotating with respect to the latter (see Figure 7). Such streamwise vortices are induced by the C-pillar vortices and are significantly weaker than the latter, as can be seen also from the results of the first row of Figure 5. While these secondary vortices are symmetrical with respect to the median plane for the headwind flow condition (Figure 7 top-left), only the leeward vortex is visible in the cross-wind conditions (Figure 7 top-right and bottom-left), due to increased intensity of the windward C-pillar vortex and the limited spatial resolution of the current measurements.

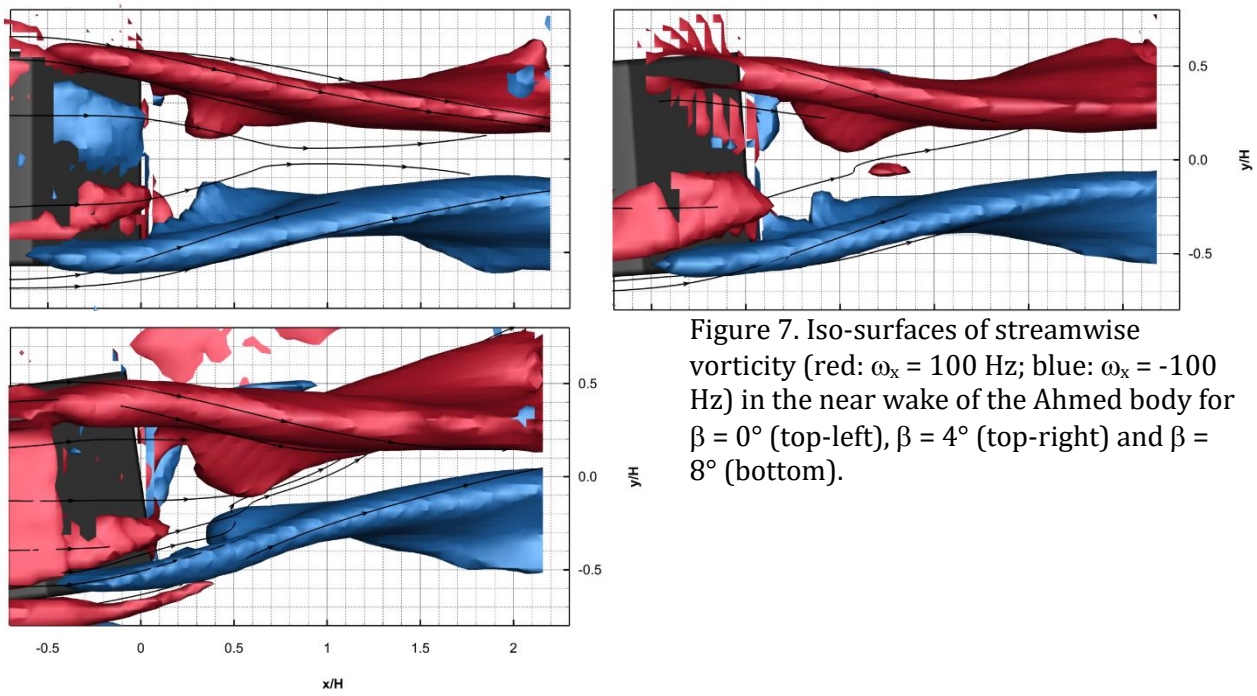

Figure 7. Iso-surfaces of streamwise vorticity (red: ω_x = 100 Hz; blue: ω_x = -100 Hz) in the near wake of the Ahmed body for β = 0° (top-left), β = 4° (top-right) and β = 8° (bottom).

For the case β = 8°, the flow field around the entire model and in its near wake has been measured, which is illustrated in Figure 8. Apart from the C-pillar vortices, the recirculation region on the slanted surface and the toroidal vortex behind the base, which have already been discussed, the flow field exhibits the presence of two roof vortical structures, emanating from both lateral sides of the model and both having positive streamwise vorticity. The windward vortex features higher strength than the leeward vortex due to the higher static pressure experienced on the windward wall of the model. On the leeward side, a ground vortex is formed due to the roll-up of the flow underneath the model towards the low-pressure leeward wall. Furthermore, a separation bubble is formed on the leeward side after the curved leading edge. Evidence of such separation is found in literature also for the headwind case, both in computational studies (Krajnović and Davidson, 2005b; Minguez et al., 2008) and experimental investigations (Zhang et al., 2015). Downstream of the model, a streamwise vortex (indicated with induced ground vortex in Figure 8) co-rotating with the windward C-pillar vortex is formed between the latter and the ground at around x/H = 0.7 and merges with the C-pillar vortex starting from x/H = 1.5. Such vortex is generated by the interaction between the flow coming from the slanted surface, and therefore directed downward, with the boundary layer lifting from the ground after the recirculation region.

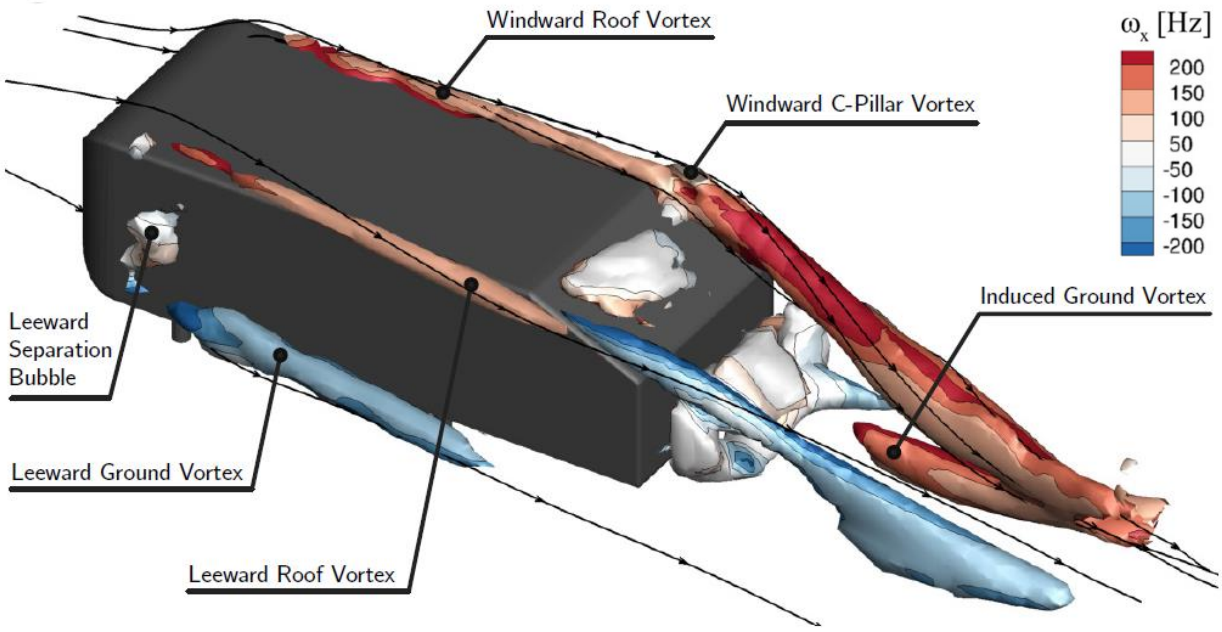

Figure 8. Flow topology around the Ahmed body at β = 8° with vortical structures visualized by iso-surfaces of Q = 4000 s^{-2} and color-coded by streamwise vorticity.

4 Conclusions

The near wake flow topology of a 25°-slant Ahmed reference body has been investigated experimentally by means of robotic volumetric PIV. Measurements have been conducted both in headwind flow conditions (β = 0°) as well as in stead cross-wind at β = 4° and β = 8°. The flow measurements show that the two C-pillar vortices, which originate at the side-edges of the beginning of the slanted surfaces, change in position and relative strength with the yaw angle. In particular, the intensity of the windward vortex increases, thus causing a stronger downwash on the windward side of the slanted surface and promoting flow reattachment. Conversely, the leeward vortex becomes weaker, causing lower downwash and therefore separated flow on the leeward side of the slanted surface. Hence, as a result of the different strength of the two C-pillar vortices, the separated region on the slanted surface becomes asymmetric. Furthermore, behind the base of the model, the windward vortex moves upwards, whereas the leeward vortex is drawn downwards and inboard. At the larger yaw angle β = 8°, the presence of an induced ground streamwise vortex is detected which co-rotates with the windward C-pillar vortex. Such ground vortex is formed at x/H = 0.7 and merges with the C-pillar vortex starting from x/H = 1.5.

References

Adrian RJ (1997) Dynamic ranges of velocity and spatial resolution of particle image velocimetry. *Measurement Science and Technology* 8:1393-1398

Agüera N, Cafiero G, Astarita T and Discetti S (2016) Ensemble 3D PTV for high resolution turbulent statistics. *Measurement Science and Technology* 27:124011

Ahmed SR (1984), Influence of base slant on the wake structure and drag of road vehicles. *Journal of Fluids Engineering* 105(4):429-434

Ahmed SR, Ramm G and Faltin G (1984) Some salient features of the time-averaged ground vehicle wake. *SAE Technical Paper* No. 840300

Bayraktar I, Landman D and Baysal O (2001) Experimental and computational investigation of Ahmed body for ground vehicle aerodynamics. *SAE paper* 2001-01-2742

Bello-Millán FJ, Mäkelä T, Parras L, del Pino C and Ferrera C (2016) Experimental study on Ahmed's body drag coefficient for different yaw angles. *Journal of Wind Engineering and Industrial Aerodynamics* 157:140-144

Hucho W and Sovran G (1993) Aerodynamics of road vehicles. *Annual Review of Fluid Mechanics* 25: 485–537

Jux C, Sciacchitano A, Schneiders JFG and Scarano F (2018) Robotic volumetric PIV of a full-scale cyclist. *Experiments in Fluids* 59:74

Keogh J, Barber T, Diasinos S and Doig G (2016), The aerodynamic effects on a cornering Ahmed body. *Journal of Wind Engineering and Industrial Aerodynamics* 154:34-46

Kourta A and Gilliéron P (2009) Impact of the automotive aerodynamic control on the economic issues. *Journal of Applied Fluid Mechanics* 2(2):69-75

Krajnović S and Davidson L (2005a) Flow around a simplified car Part 1: Large Eddy Simulation. *Journal of Fluids Engineering* 127:907

Krajnović S and Davidson L (2005b) Flow around a simplified car Part 2: Understanding the flow. *Journal of Fluids Engineering* 127:919

Lienhart H and Becker S (2003) Flow and turbulent structure in the wake of a simplified car model. *SAE Paper No.* 2003-01-0656

Lignarolo LEM, Ragni D, Krishnaswami C and Chen Q (2014) Experimental analysis of the wake of a horizontal-axis wind-turbine model. *Renewable Energy* 70:31–46

Meile W, Ladinek T, Brenn G, Reppenhagen A and Fuchs A (2016) Non-symmetric bi-stable flow around the Ahmed body. *International Journal of Heat and Fluid Flow* 57:34-47

Minguez M, Pasquetti R and Serre E (2008) High-order large-eddy simulation of flow over the "Ahmed body" car model. *Physics of Fluids* 20:095101

Schanz D, Gesemann S and Schröder A (2016) Shake-The-Box: Lagrangian particle tracking at high particle image densities. *Experiment in Fluids* 57:70

Schneiders JFG, Scarano F, Jux C and Sciacchitano A (2018) Coaxial volumetric velocimetry. *Measurement Science and Technology* 29:065201

Sciacchitano A and Scarano F (2014) Elimination of PIV light reflections via a temporal high-pass filter. *Measurement Science and Technology* 25:084009

Sellappan P, McNally J and Alvi FS (2018) Time-averaged three-dimensional flow topology in the wake of a simplified car model using volumetric PIV. *Experiments in Fluids* 59:124

Tunay T, Sahin B and Ozbolat V (2014) Effects of rear slant angles on the flow characteristics of Ahmed body. *Experimental Thermal and Fluid Science* 57:165-176

Vino G, Watkins S, Mousley P, Watmuff J and Prasad S (2005) Flow structures in the near-wake of the Ahmed model. *Journal of Fluids and Structures* 20:673-695

Wang XW, Zhou Y, Pin YF and Chan TL (2013) Turbulent near wake of an Ahmed vehicle model. *Experiments in Fluids* 54:1490

Zhang BF, Zhou Y and To S (2015) Unsteady flow structures around a high-drag Ahmed body. *Journal of Fluid Mechanics* 777:291-326